Aeroacoustic Computation of Cavity Flow in Self-Sustained Oscillations

Sung-Ryong Koh, Yong Cho, Young J. Moon*

Department of Mechanical Engineering Korea University, Seoul 136-701, Korea

A computational aero-acoustic (CAA) method is used to predict the tonal noise generated from a cavity of automobile door seals or gaps at low flow Mach numbers ($M_\infty = 0.077$ and 0.147). In the present method, the acoustically perturbed Euler equations are solved with the acoustic source term obtained from the unsteady incompressible Navier-Stokes calculations of the cavity flow in self-sustained oscillations. The aerodynamic and acoustic fields are computed for the Reynolds numbers based on the displacement thickness, $Re_{\delta^*} = 850$ and 1620 and their fundamental mode characteristics are investigated. The present method is also verified with the experimentally measured sound pressure level (SPL) spectra.

Key Words: Cavity Tone, Feedback Mechanism, CFD, Computational Aero-Acoustics (CAA)

1. Introduction

The cavity noise is a common noise source in many of the transport systems. The noise is generated by a self-sustained, periodically oscillating shear layer impinging on the downstream cavity edge. The unsteady nature of the flow is derived by a feedback mechanism; free shear layer instability, vortex roll-up, its impingement to the downstream cavity edge, and upstream propagation of fluidic/acoustic disturbances, all in a self-sustained feedback loop. Research on this subject has extensively been conducted for high speed flow applications (Roshiko, 1955; Maull and East, 1963; Rossiter, 1964; Tam, 1976; Sarohia, 1977; Tam and Block, 1978; Colonius et al., 1999) such as aircraft bomb bay, landing gear box, and etc., and the Rossiter's semi-empirical formula (Rossiter, 1964) has widely been used for data correlations.

The cavity noise is also considered as one of

* Corresponding Author,
  E-mail : yjmoon@korea.ac.kr
  TEL : +82-2-926-9290; **FAX** : +82-2-926-9290
  Department of Mechanical Engineering Korea University, Seoul 136-701, Korea. (Manuscript **Received** May 28, 2002; **Revised** November 16, 2002)

the automobile airframe noise sources. Our interest is on the tonal noise generation particularly from the automobile door seals or gaps. Figure 1 schematically illustrates a two-dimensional view of its cavity-lip configuration. The door cavity is usually exposed to the flow in the range of $100 \sim 200$ km/h ($27.8 \sim 55.6$ m/s or $M_\infty = 0.08 \sim 0.16$), a typical cruising speed in the highway. The flow speed is very low subsonic compared to the aforementioned high speed flow applications, and thereby the acoustic wavelength far exceeds the characteristic dimensions of the cavity. A mec-
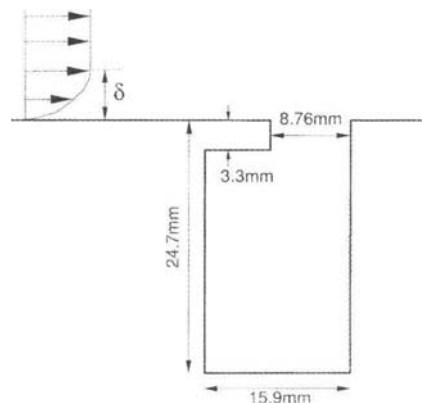
Fig. 1   An automobile door cavity-lip configuration

hanism mainly responsible for the self-sustained oscillations of the present case is the amplification of the free shear layer instability enhanced by the upstream propagating fluidic disturbances from the downstream cavity edge (Rockwell and Naudascher, 1978). An experiment was conducted by Henderson (2000) for the door cavity-lip configuration as shown in Fig. 1. In the experiment, two cases of turbulent boundary layer flows are considered for the free stream velocities of 26.8 m/s (case 1) and 50.8 m/s (case 2), and the boundary layer thickness is correspondingly 15 mm and 19 mm each at the trailing edge of the cavity lip. The tonal noise characteristics of the flow are strongly indicated by the sound pressure level (SPL) spectra measured at the left vertical wall inside the cavity.

In the present study, a computational aero-acoustic (CAA) method (Hardin and Pope, 1995 ; Shen and Sorensen, 1999) is used to numerically simulate the sound noise radiation from the door-cavity, with the acoustic source obtained by the computational fluid dynamics (CFD) calculations. For primarily concerning the effect of flow instability (Colonius et al., 1999) affected by the Reynolds number based on incoming displacement (or momentum) thickness, flows are assumed laminar with the same incoming velocities as the experiment but reducing the boundary layer thickness to 10% of the cavity base length, L. The corresponding Reynolds numbers based on the displacement thickness are 850 and 1620 and these are certainly within the range of laminar instability of the free shear layer, i.e $Re_{\delta^*} = 600 \sim 3000$. Our objectives are to simulate the aero-dynamic and aero-acoustic fields of the cavity flow, investigating their fundamental mode characteristics and to verify the present computational methods with the experimentally measured sound pressure level (SPL) spectra.

2. Computational Methodology

There exits a large disparity between the aero-dynamic scales and the acoustic ones, if the flow Mach number is close to an incompressible flow limit. For this reason, a splitting method pro-

posed by Hardin and Pope (1995) and Shen and Sorensen (1999) is employed, which decouples the direct numerical simulation (DNS) approach into an incompressible flow problem and an acoustically perturbed one. In the present study, the incompressible Navier-Stokes equations are time-accurately solved on the triangular meshes by a cell-centered based unstructured finite volume method. Then, a set of acoustically perturbed Euler equations are solved on the structured cartesian meshes with the acoustic source of time-periodic viscous flow solutions.

2.1 Unstructured incompressible flow solver algorithms

The incompressible Navier-Stokes equations in a conservative vector form are written as

$$\frac{\partial Q}{\partial t} + \frac{\partial F}{\partial x} + \frac{\partial G}{\partial y} = \frac{1}{Re} \left(\frac{\partial F_v}{\partial x} + \frac{\partial G_v}{\partial y} \right) \quad (1)$$

where

$$Q = \begin{bmatrix} 0 \\ u \\ v \end{bmatrix}, \ F = \begin{bmatrix} u \\ u^2+p \\ uv \end{bmatrix}, \ G = \begin{bmatrix} v \\ uv \\ v^2+p \end{bmatrix} \quad (2)$$

$$F_v = I_m \frac{\partial Q}{\partial x}, \ G_v = I_m \frac{\partial Q}{\partial y}, \ I_m = \begin{bmatrix} 0 & 0 & 0 \\ 0 & 1 & 0 \\ 0 & 0 & 1 \end{bmatrix} \quad (3)$$

Here a subscript v denotes the viscous terms and Re is the Reynolds number.

Equation (1) is time-accurately solved by a projection method based algorithm (Chorin, 1967 ; Hirt and Cook, 1972). The momentum equations are advanced in time by a four-stage Runge-Kutta method, and the time accurate solution is obtained by iterating the procedure between n and $n+1$ time steps, until the continuity is satisfied at each time step.

The governing equation (1) is spatially discretized on the triangular meshes by a cell-centerbased unstructured finite-volume method. The discrete form of the momentum equations is written in a conservative form as

$$A_i \frac{\Delta Q_i}{\Delta t} = - \sum_{\substack{j=g(i) \\ l=h(i,j)}} \left[\left(F - \frac{1}{Re} F_v \right) \Delta y - \left(G - \frac{1}{Re} G_v \right) \Delta x \right]_i^n \quad (4)$$

where i is a center cell index, j is a neighboring

cell index, g is a mapping relation between i and j cells, h is also a mapping relation for the cell face index l which i and j cells share, and A is a cell area. A second-order upwind differencing scheme is used for the convective flux terms in Eq. (4) by following a MUSCL approach (Van Leer, 1979), while the terms related to the viscous fluxes are treated by a centered scheme.

A discrete integral form of the Poisson equation is expressed on the triangular meshes as

$$\sum_{\substack{j=g(i)\\l=h(i,j)}} (\phi_x\Delta y - \phi_y\Delta x)_l = \sum_{\substack{j=g(i)\\l=h(i,j)}} (\hat{u}\Delta y - \hat{v}\Delta x)_l \quad (5)$$

where the gradients ϕ_x and ϕ_y at the cell face l are area-weighted between two adjacent cells i and j with each gradient obtained by the discrete surface integral.

The final form of the discretized Poisson equation is then written in an explicitform as

$$C_1\phi_i = D_i - C_2 \quad (6)$$

where

$$C_1 = \sum_{\substack{j=g(i)\\l=h(i,j)}} \left[\frac{2A_iA_j}{A_i(A_i+A_j)(A_i+A_{j'})}(\vec{s}_l\cdot\vec{s}_{l'}) - \frac{A_i-A_j}{A_i(A_i+A_j)}|\vec{s}_l| \right] \quad (7)$$

$$D_i = \sum_{\substack{j=g(i)\\l=h(i,j)}} [\hat{u}\Delta y - \hat{v}\Delta x]_l$$

$$= \sum_{\substack{j=g(i)\\l=h(i,j)}} \left[\frac{A_j\hat{u}_i+A_i\hat{u}_j}{A_i+A_j}\Delta y_l - \frac{A_j\hat{v}_i+A_i\hat{v}_j}{A_i+A_j}\Delta x_l \right] \quad (8)$$

$$C_2 = \sum_{\substack{j=g(i)\\l=h(i,j)}} \left[\frac{\vec{s}_l\cdot\vec{s}_{l'}}{A_i+A_{j'}(A_i+A_{j'})}(A_j\phi_j+A_{j'}\phi_{j'}) - \frac{A_i-A_j}{A_i(A_i+A_j)}|\vec{s}_l|\phi_j \right]$$
$$+ \sum_{\substack{j=g(i)\\l=h(i,j)}} \left[\frac{A_i}{A_j(A_i+A_j)}\left(\sum_{\substack{k=g(j),k\neq i\\m=h(j,k)}} \frac{A_k\phi_j+A_j\phi_k}{A_j+A_k}(\vec{s}_l\cdot\vec{s}_m) \right) \right] \quad (9)$$

and $\vec{s}_l$ represents a vector tangent to the cell face l with a magnitude ofthe cell face length, j' denotes a center cell index sequential to j according to the mapping relation $g(i)$, and l' is a cell face index defined in the same manner as j'. Figure 2 shows a schematic of the numerical stencil (10 cells) and index definitions used in Eq. (4). The Poisson equation is then iteratively solved by a pointwise Gauss-Seidel method. For the intermediate velocities at the cell faces in Eq. (5) or (8), averaging the velocities of two adjacent cells i and j would result in an odd-even
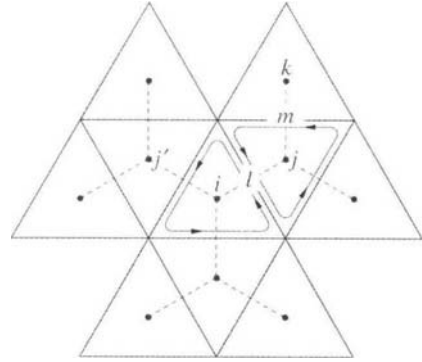

Fig. 2   Numerical stencil and index definitions for the discretized Poisson equation in unstructured grid formulation

decoupling of the pressure field. Therefore the velocities at the cell faces are re-defined by a momentum interpolation technique used by Rhie and Chow (1983).

2.2   Computational aero-acoustic algorithms

The acoustic fields are computed by a splitting method proposed by Shen and Sorensen (1999). The instantaneous velocities, pressure, and density are decomposed into the hydrodynamic variables at a mean-state and the acoustically perturbed quantities denoted by a prime,

$$u_i = U_i + u_i'$$
$$p = P + p' \quad (10)$$
$$\rho = \rho_0 + \rho'$$

Inserting the decomposed variables into the compressible Navier-Stokes equations, a set of acoustic field equations are derived by subtracting the incompressible Navier-Stokes equations from them ;

$$\frac{\partial\rho'}{\rho t} + \frac{\partial f_i}{\partial x_i} = 0 \quad (11)$$

$$\frac{\partial f_i}{\partial t} + \frac{\partial}{\partial x_j}[f_i(U_j+u_j')+\rho_0 U_iu_j'+p'\delta_{ij}] = 0 \quad (12)$$

$$\frac{\partial p'}{\partial t} + c^2\frac{\partial f_i}{\partial x_i} = -\frac{\partial P}{\partial t} \quad (13)$$

where $f_i = \rho u_i' + \rho'U_i$, $c^2 = \gamma p/\rho$, and $\gamma = 1.4$ is a ratio of specific heats.

Equations (11)-(13) are numerically solved by

the second-order accurate MacCormack's predictor-corrector scheme, in coupled with the unsteady incompressible flow computations. The acoustic field calculation can be started with an initial condition $(\rho'=u'=v'=p'=0)$ anytime after a periodically oscillating flow solution is obtained. For the present scheme, 20~25 mesh points are used per one acousitc wavelength, which is strictly required in order to properly resolve the wave propagation with the least numerical diffusion and dispersion errors (Hardin and Pope, 1995). In the computation, a fourth-order artificial dissipation term is also added to Eqs. (11)-(13) to stabilize the numerical scheme. The numerical accuracy of the present splitting method was validated by Shen and Sørenson (Shen and Sørenson, 1999).

In computational acoustics, the problems involving wave reflections are issued very importantly because the physical domains are necessarily truncated due to the limitation of a finite computational domain. Thus, at these artificial boundaries, non-reflecting or absorbing numerical boundary conditions are needed so that outgoing waves are not reflected into the computational domain. In the far-field buffer zones, the Perfectly-Matched Layer (PML) equations (Hu, 1996) are applied by splitting each of the flow variables $(\rho'=\rho_1'+\rho_2')$ and by segregating the spatial gradients into each split equation (the ρ_1' equation only includes the x_1-gradients). for example, Eq. (11) is written as

$$\frac{\partial \rho_1'}{\partial t} + \sigma_x \rho_1' + \frac{\partial f_1}{\partial x_1} = 0$$
$$\frac{\partial \rho_2'}{\partial t} + \sigma_y \rho_2' + \frac{\partial f_2}{\partial x_2} = 0 \tag{14}$$

The damping parameters are defined as

$$\sigma_x = \sigma_m \left(\frac{|x - x_0|}{D} \right)^\beta$$
$$\sigma_y = \sigma_m \left(\frac{|y - y_0|}{D} \right)^\beta \tag{15}$$

where σ_m and β are the damping coefficients, and the thickness of the PML domain D is defined such that x_0 and y_0 are the location of the interface between the interior and PML domains.

3. Computational Results and Discussion

3.1 Computational details

Two cases of laminar boundary layer flows with free stream velocities of 26.8 m/s and 50.8 m/s are computed for the cavity-lip configuration as shown in Fig. 1. The flow is air and the boundary layer thickness is 10% of the cavity base length (L) at the trailing edge of the cavity lip. The Reynolds numbers based on the displacement thickness, Re_{δ^*} are correspondingly 850 and 1620. The dimensions of the cavity-lip configuration are presented in Fig. 1 and all the length scales are normalized by the cavity base length in the computation.

Figure 3 shows the computational meshes consisted of 11,240 triangular cells, which basically comprises the upstream boundary layei, cavity, and downstream region. One hundred and ten points are distributed in the streamwise direction for the upstream region, where a boundary layer develops into a thickness close to $0.1L$ at the

(a) Global view of the cavity-lip configuration

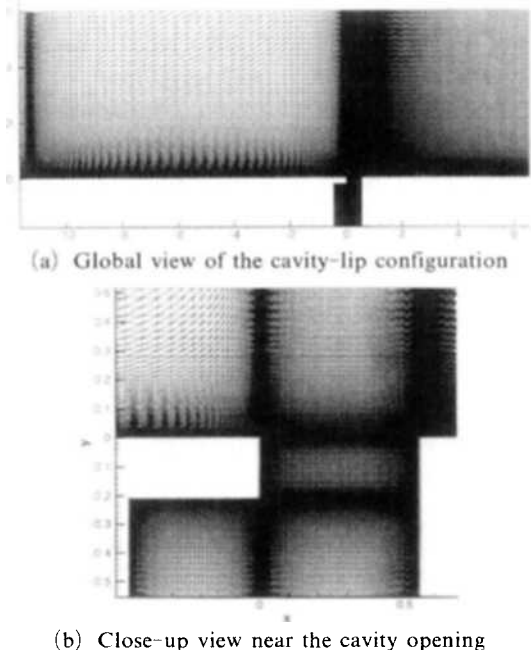(b) Close-up view near the cavity opening

Fig. 3 Computational meshes (11,240 triangular elements)

trailing edge of the lip. A uniform flow is used as an inflow boundary condition, although this region could be shorten by imposing a Blasius solution along the inflow boundary. From the numerical exercises, however, there exit some cases where the pressure waves propagating from the downstream cavity edge makes the upstream boundary layer unfavorable or sometimes separated. Therefore, a full inclusion of the boundary layer was necessary, instead of enforcing aprescribed inflow boundary condition.

As it was mentioned, the feedback mechanism is generated by the upstream propagating fluidic disturbances from the downstream cavity edge and the subsequent enhancements of the vortex shedding from the trailing edge of the lip. Therefore, the mesh resolution around the cavity-lip is very important. In the present computation, 40 points are used across the lip, 60 points along the lip, 80 points along the cavity opening, and 100 points along the leftvertical wall inside the cavity. The mesh details around this region are shown in Fig. 3(b). Also, for resolving the instability of the free shear layer, a minimal normal spacing of 0.001 from the wall is used for the case 1, and 0.0005 for the case 2, with 100 points distributed in the y-direction from the wall to the top boundary.

For the downstream region, 200 mesh points are distributed to resolve the convection of the vorticity waves. It is of our concern that improper numerical damping of vorticity waves may have an upstream-effect on the time-dependent accuracy of the flow. This will further be discussed in Section 2.2. One other important element is also the treatment of the outflow boundary condition. In the present study, a convective boundary condition (Pauley et al., 1990) was imposed along the outflow boundary for the proper wave transmission. For example, a quasi one-dimensional wave equation $\partial\phi/\partial t + c\partial\phi/\partial x = 0$ is solved numerically at the boundary, where ϕ is either u or v and a local streamwise velocity at one grid point upstream from the boundary is used for the local wave speed c.

3.2 Cavity flow in self-sustained oscillations

The computational results of self-sustained, periodically oscillating flow over the cavity are presented. Figure 4 shows the time-periodic solutions of vorticity contours for the case 1 at its shear layer mode one. Figure 4(a), at $\tilde{t} = tU_\infty/L = 35.9$, corresponds to the cavity at the expansion mode, while Fig. 4(b), 0.41 T apart from 4(a), is at the compression mode. One can also see the propagation of vorticity waves shed from the downstream cavity edge. A time-dependent flow characteristics of the normal component v-velocity right before the downstream cavity edge is presented in Fig. 5. The period of oscillation computed for the case 1 is 1.47 (in a non-dimensional time), which corresponds to $St = fL/U_\infty = 0.68$, or $f = 1215$ Hz. The case 2 also exhibits a solution at the shear layer mode one, which corresponds to a period of 1.55 ($St = 0.65$ or $f = 2080$ Hz). The fundamental mode flow characteristics of both case 1 and 2 will later be confirmed by the experimental data in Fig. 10.

The periodicity of self-sustained oscillations of the flow is well captured with the present computational meshes (called grid-A), although this computation is quite sensitive to the grid resolu-
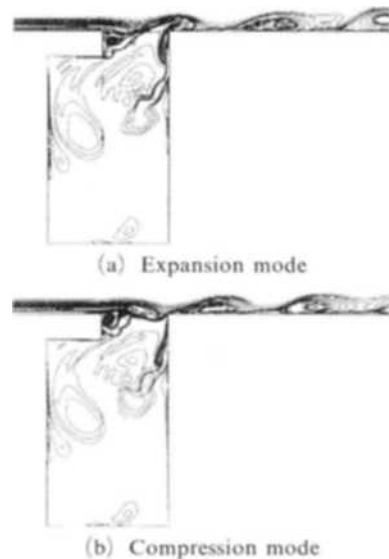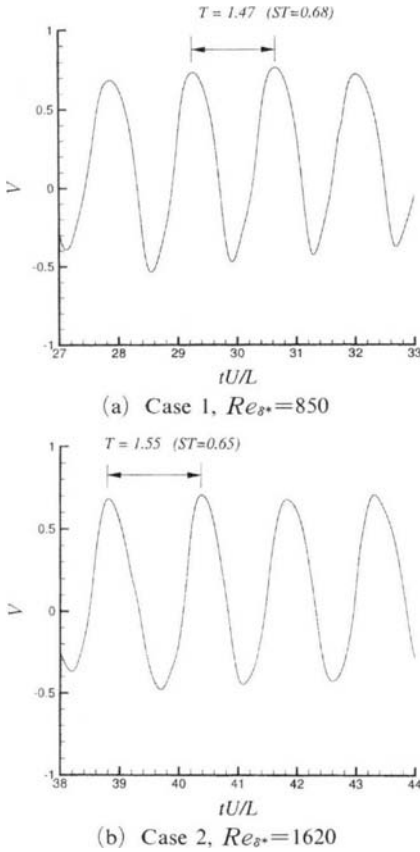

(a) Expansion mode

(b) Compression mode

Fig. 4 Instantaneous vorticity contours (Case 1, $Re_{\delta^*} = 850$)

(a) Case 1, $Re_{\delta*}=850$

(b) Case 2, $Re_{\delta*}=1620$

Fig. 5 Time-dependent flow characteristics at the fundamental mode (v-velocity)

(a) Grid-B

(b) Grid-C

Fig. 6 Grid sensitivity test (Case 1, v-velocity)

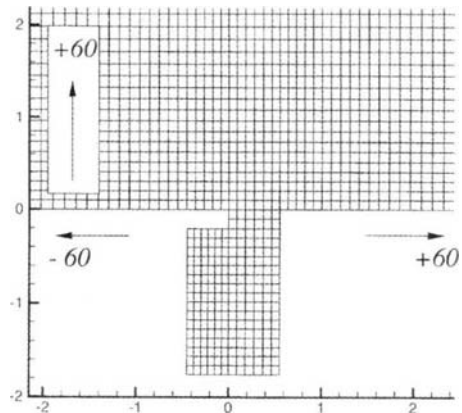**Fig. 7** Cartesian meshes for the acoustic field computation

tion parameters. The grid sensitivity tests have been conducted ; (i) by doubling the minimum normal grid spacing at the wall (called grid-B) and (ii) in addition to (i), by halving the grid points in the streamwise direction for the downstream region (called grid-C). The computed results of v-velocity at the downstream cavity edge are presented in Fig. 6, showing that the periodicity of oscillation starts to break from the grid-B calculation and becomes even worse on the grid-C. The grid sensitivity tests seem to indicate that the grid resolution in the downstream region could impose different numerical impedances to the vorticity waves and consequently have an upstream-effect on the oscillations of the shear layer.

3.3 Tonal noise

A tone generated by the self-sustained oscilla-

tions of the shear layer over the cavity is computed by using the cartesian meshes shown in Fig. 7. Since the flow Mach number of the case 1 is 0.077 and the computed Strouhal number of the flow oscillation is 0.68, the acoustic wavelength
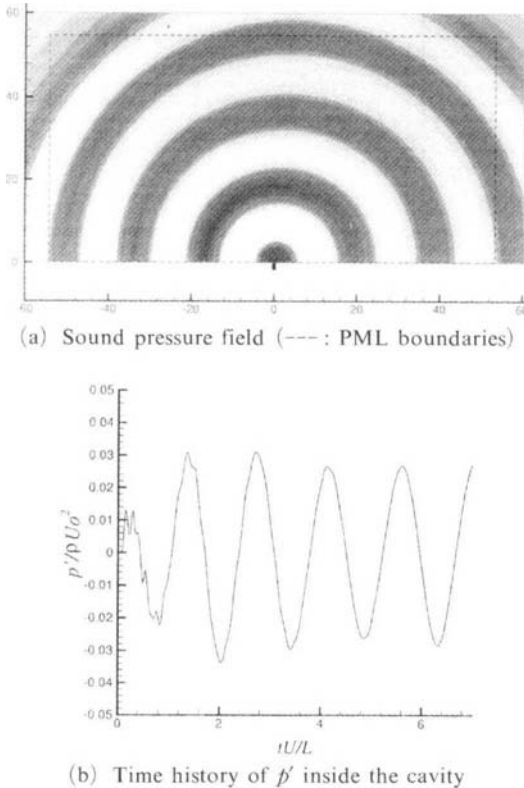
(a) Sound pressure field (--- : PML boundaries)

(b) Time history of p' inside the cavity

Fig. 8 Tonal noise radiation (Case 1, $M_\infty = 0.077$)

(a) Sound pressure field

(b) Time history of p' inside the cavity

Fig. 9 Tonal noise radiation (Case 2, $M_\infty = 0.147$)

of the radiated tone can approximately be estimated as 19 based on the relation of $\lambda/L = 1/(St \cdot M_\infty)$. The acoustic computational domain is therefore stretched out to $60L$ to include 2 or 3 wavelengths of the sound waves. The number of grid points for the acoustic field computation is determined by the fact that $20 \sim 25$ pointsbe included per wavelength, in order to minimize the numerical dispersion and dissipation errors of the MacCormack's second-order scheme (Hardin and Pope, 1995).

The computed sound pressure field is presented in Fig. 8(a), where the dotted line indicates the boundaries of the PML zones. The shaded flooding contours well illustrate the sound wave radiations from the automobile door cavity. Notice that the cavity is shown as a little tiny prong near the origin of the coordinate. The computed acoustic wavelength is $18 \sim 18.5$, close to the estimated value of 19, and the highest intensity of the radiated sound noise is between $135° \sim 180°$. The

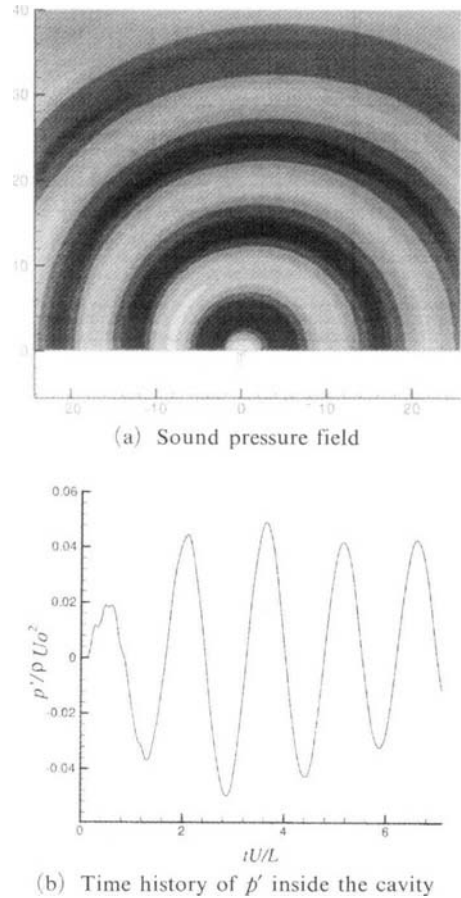cavity inside experiences a lateral mode of compression and expansion, as the shed vortex from the lip rolls up and impinges off the downstream cavity edge, alternately. Figure 8(b) shows the time history of the sound pressure at the center of the left vertical wall inside the cavity, and the predicted sound pressure level (SPL) of the tonal noise is 118 dB at 1215 Hz. The sound pressure level is obtained by $SPL(dB) = 20 \log \dfrac{p'_{rms}}{p_{ref}}$, where $p_{ref} = 2 \times 10^{-5}$ Pa. Even though the computational flow condition (thin laminar boundary layer) is somewhat different from the experiment (relatively thick turbulent boundary layer), quantitative comparison is within the range. As shown in Fig. 10, the measured SPL spectra indicate that the case 1 at very low flow Mach number of $M_\infty = 0.077$ seems to experience
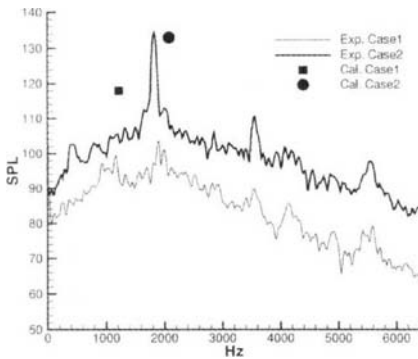
Fig. 10 Sound pressure level spectra (Case 1 & 2, Exp.: Henderson (2000))

a dual shear layer mode of one or two. Therefore, the tonal noise characteristic is not so strong as the case 2. The computed frequency is quite closely compared with experiment at the mode one, although the sound pressure level was somewhat over-predicted.

The computational result of the case 2 ($St=$ 0.65 or 2080 Hz) is presented in Fig. 9. As shown in Fig. 9(a), the computed acoustic wavelength is 9.5, quite close to the estimated value of 10. Figure 9(b) also shows the time history of p' at the left cavity wall, predicting the SPL of 133 dB. The tonal noise frequency and SPL of the case 2 are quite closely compared with experiment in Fig. 10. In comparison with the case 1, the fundamental mode characteristic is more evident, due to the increased compressibility effect at the flow Mach number of $M_\infty=0.147$.

4. Conclusions

A tonal noise from a cavity of automobile door seals or gaps is computed by a computational aero-acoustic (CAA) algorithm, acquiring the acoustic source from the unsteady incompressible Navier–Stokes calculations of the cavity flow in self-sustained oscillations.

The aerodynamic calculations of the cavity flow involving feedback are found to be quite sensitive to the mesh resolution around the cavity opening, due to the fact that the excitation of the free shear layer instability is strongly coupled with the upstream propagating fluidic distur-

bances generated from the downstream cavity edge. Numerical difficulties were also encountered in capturing the time-periodic behavior of the flow, without properly resolving the downstream propagating vorticity waves and their transmissions through the outflow boundary.

The acoustic fields of the cavity flow are successfully computed by the present CAA method for the low Mach numbers of $M_\infty=0.077$ and 0.147. The wavelengths and frequencies of the case 1 and 2 are quite favorably compared with the experimentally measured frequency spectra at the shear layer mode one. The sound pressure level of the tonal noise predicted by the CAA method is also closely matched with the experiment of case 2, while the SPL of the case 1 is somewhat over-predicted due to the less evident fundamental mode characteristic of the cavity flow.

Acknowledgment

References

Chorin, A. J., "A Numerical Method for Solving Incompressible Viscous Flow Problems," *J. Comput. Phys.*, Vol. 2, pp. 12~26.

Colonius, T., Basu, A. J. and Rowley, C. W., 1999, "Numerical Investigation of the Flow pasta Cavity," *AIAA Paper* 99-1912.

Hardin, J. C. and Pope, D. S., 1995, "Sound Generation by Flow over a Two-dimensional Cavity," *AIAA J.*, Vol. 33, pp. 407~412.

Henderson, B., 2000, "Automobile Noise Involving Feedback-sound Generation by Low Speed Cavity Flows," *Third Computational Aeroacoustics (CAA) Workshop on Benchmark Problems*, NASA/CP-2000-209790.

Hirt, C. W. and Cook, J. L., 1972, "Calculating Three-dimensional Flows around Structures and over Rough Terrain," *J. Compt. Phys.*, Vol. 10, pp. 324~340.

Hu, F. Q., 1996, "On Absorbing Boundary

Conditions for Linearized Euler Equations by a PML," *J. Compt. Phys.*, Vol. 129, pp. 201~219.

Maull, D. J. and East, L. F., 1963, "Three-Dimensional Flow in Cavities," *J. Fluid Mech.*, Vol. 16, pp. 620~632.

Pauley, L. L., Moin, P., and Reynolds, W. C., "The Structure of Two-Dimensional Separation, "*J. Fluid Mech.*, Vol. 220, pp. 397~441.

Rhie, C. M. and Chow, W. L., 1983, "Numerical Study of the Turbulent Flow past an Airfoil with Trailing Edge Separation," *AIAA J.*, Vol. 21, pp. 1525~1532.

Rockwell, D. and Naudascher, E., 1978, "Review-Self-sustaining Oscillations of Flow past Cavities," *J. Fluids Eng.*, Vol. 100, pp. 152~165.

Roshko, A., 1955, "Some Measurements of Flow in a Rectangular Cutout," *NACA TN-3488*.

Rossiter, J. E., 1964, "Wind-tunnel Experiments on the Flow over Rectangular Cavities at Subsonic and Transonic Speeds," *Aeronautical Research Council Reports and Memoranda*, Technical report 3438.

Sarohia, V., 1977, "Experimental Investigation of Oscillations in Flows over Shallow Cavities," *AIAA J.*, Vol. 15, pp. 984~991.

Shen, W. Z. and Sørensen J. N., 1999, "Aeroacoustic Modelling of Low-Speed Flows," *Theoretical and Computational Fluid Dynamics*, Vol. 13, pp. 271~289.

Tam, C. K., 1976, "The Acoustic Modes of a Two-dimensional Rectangular Cavity," *J. Sound and Vibration*, Vol. 49, pp. 353~364.

Tam, C. K. W. and Block, P. J. W., 1978, "On the Tones and Pressure Oscillations Induced by Flow over Rectangular Cavities," *J. Fluid Mech.*, Vol. 89, pp. 373~399.

Van Leer, B., 1979, "Towards the Ultimate Conservative Difference Schemes V-A Second Order Sequel to Godunov's Method," *J. Compt. Phys.*, Vol. 32, pp. 101~136.